Available online at www.sciencedirect.com
ScienceDirect
International Journal of Heat and Mass Transfer 50 (2007) 3848–3861
International Journal of HEAT and MASS TRANSFER
www.elsevier.com/locate/ijhmt

Large-eddy simulation of combined forced and natural convection in a vertical plane channel

Jing Yin [a], Bing-Chen Wang [b,1], Donald J. Bergstrom [a,*]

[a] Department of Mechanical Engineering, University of Saskatchewan, Saskatoon, Saskatchewan, Canada S7N 5A9
[b] Defence R&D Canada–Suffield, STN Main, P. O. Box 4000, Medicine Hat, Alberta, Canada T1A 8K6

Received 27 June 2006; received in revised form 5 February 2007
Available online 16 April 2007

Abstract

A combined forced and natural convective flow between two vertical plates with different temperatures is studied using large eddy simulation. The numerical simulations were performed with a Grashof number of $Gr = 9.6 \times 10^5$ and Reynolds number of $Re_\tau = 150$ (based on the wall friction velocity and half channel width). Two sets of dynamic subgrid-scale (SGS) models were tested in the simulation; namely, the set of linear SGS models consisting of the dynamic Smagorinsky SGS stress model (DM) and dynamic eddy diffusivity SGS heat flux model (DEDM-HF), and the set of nonlinear SGS models consisting of the dynamic nonlinear SGS stress model (DNM) and dynamic tensor diffusivity SGS heat flux model (DTDM-HF). The numerical results are compared with the reported direct numerical simulation data. It is found that the resolved and SGS quantities related to the temperature field are noticeably influenced by the choice of SGS models. In general, the set of dynamic nonlinear SGS models yields better prediction of the flow than the set of dynamic linear SGS models.

Keywords: Turbulence; Convection; Buoyancy; Heat transfer; Large-eddy simulation; Subgrid-scale model

1. Introduction

In mechanical and environmental engineering, combined (mixed) forced and natural turbulent convection is a frequently encountered thermal-fluid phenomenon, which exists, for example, in the atmospheric environment, urban canopy flows, ocean currents, gas turbines, heat exchangers, nuclear reactors, and computer chip cooling systems. In the early development of the subject of convective heat transfer, forced and natural convections were studied separately and the interaction between these two physical processes was ignored. Modern research on combined forced and natural convection was initiated in the 1960's based on experimental approaches (see Metais and Eckert [1]). Since then, refined experimental measurements have become available [2,3], and the research methodology has been extended to numerical simulations based on the Reynolds averaged Navier–Stokes (RANS) method [4,5] and direct numerical simulations (DNS) [6]. A detailed review of the subject (up to 1989) can be found in Jackson et al. [7]. Recently, large-eddy simulation (LES) has been utilized for studying this type of flow, which includes the work of Lee et al. [8] who studied a heated vertical annular pipe flow, that of Zhang and Chen [9] who studied indoor air flows, that of Yan [10] who investigated thermal plumes for different initial conditions, that of Tyagi and Acharya [11] who studied heat transfer in a rotating channel flow with rib turbulators, and that of Wang et al. [12] who studied combined forced and natural convective channel flow using a general dynamic linear tensor thermal diffusivity (or simply, tensor diffusivity) subgrid-scale heat flux model.

By their nature, buoyancy driven turbulent flows are unsteady and feature both large and fine scale flow

* Corresponding author. Tel.: +1 306 966 5454; fax: +1 306 966 5427.
E-mail addresses: bingchen.wang@drdc-rddc.gc.ca (B.-C. Wang), jiy080@mail.usask.ca, don.bergstrom@usask.ca (D.J. Bergstrom).
[1] Tel.: +1 403 544 4791; fax: +1 403 544 3388.

0017-9310/$ - see front matter © 2007 Elsevier Ltd. All rights reserved.
doi:10.1016/j.ijheatmasstransfer.2007.02.014

Nomenclature

a_j, b_j	base vectors
C_f	resolved friction coefficient: $2\tau_w/\rho U_D^2$
c_P	specific heat at constant pressure
C_S, C_W, C_N	SGS stress model coefficients
C_θ^T	SGS heat flux model coefficient
D	distance from the wall to the maximum streamwise velocity location
D_{ij}	tensor thermal diffusivity
g_i	gravitational acceleration vector: $[-g, 0, 0]^T$
Gr	Grashof number: $g\beta\Delta\theta(2\delta)^3/\nu^2$
h_j	grid level SGS heat flux vector
H_j	test-grid level SGS heat flux vector
$\mathscr{L}_{ij}$	Leonard type stress tensor
$\mathscr{L}_j$	vector
M_{ij}, W_{ij}, N_{ij}	differential tensors
M_j	differential vector
Nu	Nusselt number: $2q_w/[\lambda(\theta_D - \theta_w)/D]$
p	pressure
q_w	wall heat flux
Re_τ	Reynolds number based on friction velocity: $u_\tau\delta/\nu$
Re_b	Reynolds number based on bulk velocity: $U_b\delta/\nu$
$\overline{S}_{ij}$	resolved strain rate tensor: $(\partial\bar{u}_i/\partial x_j + \partial\bar{u}_j/\partial x_i)/2$
T_τ	wall friction temperature: $q_w/(\rho c_P u_\tau)$
T_{ij}	test-grid level SGS stress tensor
U_b	bulk velocity across the channel: $\int_0^{2\delta}\langle\bar{u}_1\rangle\,dx_2/(2\delta)$
U_D	bulk velocity averaged over the distance D: $\int_0^D\langle\bar{u}_1\rangle\,dx_2/D$
u_i	velocity components: $i = 1, 2, 3$
u_τ	wall friction velocity: $\sqrt{\tau_w/\rho}$
α	molecular thermal diffusivity: $\lambda/(\rho c_P)$
α_{sgs}	SGS eddy thermal diffusivity
α_{ij}, γ_{ij}, η_{ij}	grid level tensors
β	thermal expansion coefficient
β_{ij}, λ_{ij}, ζ_{ij}	test-grid level tensors
δ	half channel width
δ_{ij}	Kronecker delta
Δ	mesh or filter length
Γ	effective eddy diffusivity for turbulent heat flux
λ	thermal conductivity
ν	kinematic viscosity
ν_{sgs}	SGS eddy viscosity
$\overline{\Omega}_{ij}$	resolved rotation rate tensor: $(\partial\bar{u}_i/\partial x_j - \partial\bar{u}_j/\partial x_i)/2$
ρ	density
σ_{sgs}	SGS Prandtl number
θ	temperature
θ_b	bulk temperature across the channel: $\int_0^{2\delta}\langle\bar{\theta}\rangle\,dx_2/(2\delta)$
θ_D	bulk temperature averaged over the distance D: $\int_0^D\langle\bar{\theta}\rangle\,dx_2/D$
Θ_r	reference temperature
τ_w	wall shear stress
τ_{ij}	grid level SGS stress tensor
ϕ	a function of space

Subscripts and Superscripts

$(\cdot)_1$	streamwise component
$(\cdot)_2$	wall-normal component
$(\cdot)_3$	spanwise component
$(\cdot)^a$	averaged value over two walls
$(\cdot)_c$	value at cold wall
$(\cdot)_h$	value at hot wall
$(\cdot)_i$, $(\cdot)_j$, $(\cdot)_{ij}$	vectors or tensors: $i, j = 1, 2, 3$
$(\cdot)_{ij}^*$	a trace-free tensor: $(\cdot)_{ij}^* = (\cdot)_{ij} - (\cdot)_{kk}\delta_{ij}/3$
$(\cdot)_{rms}$	root-mean-square
$(\cdot)_{sgs}$	subgrid-scale component
$(\cdot)_w$	value at the wall
$\overline{(\cdot)}$	grid level filter
$\widetilde{(\cdot)}$	test-grid level filter
$(\cdot)^+$	wall coordinates
$(\cdot)''$	residual component relative to a time- and plane-averaged quantity
$\langle\cdot\rangle$	time- and plane-averaged quantity

structures. Therefore, in comparison with the RANS method which is based on the concept of ensemble averages, a time dependent and fine scale resolved calculation based on DNS or LES can provide more details of the temperature and fluid flow fields. In LES of buoyant flows, the unknown subgrid-scale (SGS) stress tensor and heat flux (HF) vector associated with the unresolved scales of motion need to be modelled to close the set of governing equations. Although in a direct sense, the SGS stress model is for closing the filtered momentum equation and the SGS HF model is for closing the filtered thermal energy equation, these two types of SGS models jointly influence both the velocity and temperature fields. This is because the transport of momentum is tightly coupled with that of thermal energy in a combined forced and natural convective flow, temporally and spatially. In the following context, we briefly review the SGS stress and HF modelling approaches that are relevant to this research.

The conventional Smagorinsky type Dynamic model (DM) introduced by Germano et al. [13] and Lilly [14] is known for its capability of self-calibration, general balancing of the turbulence kinetic energy (TKE) between the resolved and unresolved scales, and being free from any empirical constants and artificial near-wall damping functions. However, the DM originates from the Smagorinsky constitutive relation which is based on the molecular transport analogy and requires the principal axes of the negative SGS stress tensor to be strictly aligned with those of the

filtered strain rate tensor. This rigid and over-simplified geometrical relation between the stress and strain rate tensors is not realistic in terms of physics and can cause a series of potential problems. For instance, simulations based on the DM can be numerically unstable due to excessive backscatter of TKE from the subgrid to resolved scales if the model coefficient is not properly bounded [15]. The DM is difficult to be applied locally without plane averaging the model coefficient [13,14] for a plane channel flow; and on the other hand, localization of the DM often results in integral equations which are difficult and costly to solve [16]. Since the above mentioned deficiencies related to the DM stem from its over-simplified constitutive relation, improved dynamic SGS stress models often consider non-Smagorinsky type constitutive relations. One of the important approaches to achieve this goal is to use explicit nonlinear tensor functions to build the constitutive relation, which is represented by the recent works of Lund and Novikov [17], Wong [18], Kosović [19], Winckelmans et al. [20], Liu et al. [21], and Wang and Bergstrom [22]. The dynamic nonlinear model (DNM) proposed by Wang and Bergstrom [22] is based on the three-parameter quadratic constitutive relation of Speziale and Gatski [23,24]. It is observed that in comparison with the conventional DM, the DNM can significantly increase the numerical stability and can be implemented in the simulation locally without using the plane averaging technique; it also allows for a more realistic geometrical representation of the SGS stress tensor [25] and provides more degrees of freedom for reflecting both forward and backward scatter of TKE between the resolved and unresolved scales. In this paper, we use both the conventional DM and the recently proposed DNM for closure of the filtered momentum equation, and the performances of these two models are compared in terms of their prediction of the resolved thermal-fluid flow fields.

In order to close the filtered thermal energy transport equation, the issue of SGS heat flux modelling needs to be addressed. The concept of the dynamic SGS heat flux (or, in a general sense, SGS scalar flux) modelling was initially introduced by Moin et al. [26] in 1991 soon after the proposal of the dynamic procedure by Germano et al. [13]. The central idea of the dynamic SGS HF modelling approach in the pioneering work of Moin et al. [26] is based on the concept of a linear eddy thermal diffusivity (or simply, eddy diffusivity), which assumes that the SGS HF vector h_j is instantaneously proportional to and aligned with the negative resolved temperature gradient $\partial\bar{\theta}/\partial x_j$, viz. $h_j \propto -\partial\bar{\theta}/\partial x_j$. This linear constitutive relation is based on the analogy to the molecular heat diffusion/conduction process governed by Fourier's law. Since the transport of the SGS thermal energy due to unresolved turbulent motions is fundamentally different and much more complex than that due to a molecular heat conduction process, it is understood that the conventional dynamic eddy thermal diffusivity SGS HF model (DEDM-HF) as introduced by Moin et al. [26] cannot correctly reflect the geometrical property of the SGS HF vector as required by the physics of turbulence, and this has been confirmed by the recent study of Abe and Suga [27]. Nevertheless, the DEDM-HF is still the most popular model in literature and has been successfully applied for predicting the mean properties of the turbulent scalar fields [28–36]. Here, we use a suffix "-HF" to indicate a SGS HF model, so that the abbreviation for a SGS HF model can be differentiated from that for a SGS stress model.

In order to improve the performance of the SGS HF model in terms of its physical and geometrical representation of the SGS HF vector, some innovative modelling approaches have been proposed in the literature. Using a statistical approach, Yoshizawa [37] derived a SGS HF model based on the gravitational acceleration vector and resolved temperature and velocity gradients (it should be noted that Yoshizawa's model does not rely on the dynamic modelling approach, which is different than the SGS HF models to be discussed below). Salvetti and Banerjee [38] introduced a dynamic two-parameter mixed SGS HF model (DTPMM-HF), which dynamically combines the linear eddy diffusivity SGS HF model with a scale-similarity SGS HF model. The proposed DTPMM-HF of Salvetti and Banerjee was an extension of the work of Zang et al. [39] on a dynamic mixed SGS stress model, and has been recently applied by Tyagi and Acharya [11] for studying heat transfer of rotating rib roughened square duct flow, and by Jaberi and Colucci [40] for studying reacting and non-reacting turbulent flows using both the *a priori* and *a posteriori* LES methods. Based on a Taylor series analysis of the discrete filtering process related to the SGS heat flux term, Porté-Agel et al. [41,42], and Kang and Meneveau [43] introduced a simplified DTPMM-HF, which dynamically combines the linear eddy diffusivity SGS HF model with a gradient SGS HF model. The simplified DTPMM-HF of Porté-Agel et al. [41,42], and Kang and Meneveau [43] has been applied for studying heat fluxes and dissipation in an atmospheric boundary layer and heated wind tunnel wake flow using the *a priori* LES approach. Using the theory of tensor functions, Wang et al. [12] recently proposed an dynamic inhomogeneous linear tensor diffusivity model (DILTDM-HF) for studying a mixed convective channel flow. The tensor diffusivity for the DILTDM-HF is constructed as an inhomogeneous linear function of the resolved strain rate and rotation rate tensors. Peng and Davidson [44] proposed a dynamic tensor diffusivity SGS HF model (DTDM-HF) for studying buoyant turbulent flow. The DTDM-HF of Peng and Davidson replaces the dynamic eddy diffusivity (which is a scalar function) introduced by Moin et al. [26] with a tensor function based on the resolved strain rate tensor, viz. $h_j \propto -\overline{S}_{jk}(\partial\bar{\theta}/\partial x_k)$. Since the unphysical parallel alignment between h_j and $-\partial\bar{\theta}/\partial x_j$ as rigidly imposed by the DEDM-HF is abandoned in both the DILTDM-HF and DTDM-HF, these two models are expected to be able to provide a more realistic geometrical representation of h_j.

The combined forced and natural convective flow to be studied using the LES method in this research is based on the benchmark DNS test case of Kasagi and Nishimura [6]. In this research, we focus our attention on evaluation of the performance of the linear and nonlinear SGS models in terms of their capability for predicting the resolved thermal-fluid flow fields. In particular, we compare the set of linear SGS models based on the DM [14] (for modelling τ_{ij}) and DEDM-HF [26] (for modelling h_j), with the set of nonlinear SGS models based on the DNM [22] (for modelling τ_{ij}) and DTDM-HF [44] (for modelling h_j). This paper is organized as follows: in Section 2, the mathematical equations for the SGS stress and HF models are introduced; in Section 3, the test case and numerical method are described; in Section 4, the numerical results obtained using different SGS models are compared with the DNS study of Kasagi and Nishimura [6], Kuroda et al. [45] and Davidson et al. [46]; and finally in Section 5, conclusions of this research are summarized.

2. Mathematical models

In LES, the system of equations governing the heat and fluid flow for incompressible fluids are obtained by applying a filtering operation to the continuity, momentum and thermal energy equations:

$$\frac{\partial \bar{u}_i}{\partial x_i} = 0, \tag{1}$$

$$\frac{\partial \bar{u}_i}{\partial t} + \frac{\partial}{\partial x_j}(\bar{u}_i\bar{u}_j) = -\frac{1}{\rho}\frac{\partial \bar{p}}{\partial x_i} + \nu\frac{\partial^2 \bar{u}_i}{\partial x_j \partial x_j} - \frac{\partial \tau_{ij}}{\partial x_j} - \beta g_i(\bar{\theta} - \Theta_r), \tag{2}$$

$$\frac{\partial \bar{\theta}}{\partial t} + \frac{\partial}{\partial x_j}(\bar{u}_j\bar{\theta}) = \alpha\frac{\partial^2 \bar{\theta}}{\partial x_j \partial x_j} - \frac{\partial h_j}{\partial x_j}, \tag{3}$$

where $\tau_{ij} \overset{\text{def}}{=} \overline{u_i u_j} - \bar{u}_i\bar{u}_j$ and $h_j \overset{\text{def}}{=} \overline{u_j\theta} - \bar{u}_j\bar{\theta}$ are the SGS stress tensor and HF vector, respectively. The appearance of these two terms is due to the filtering process. They represent the effect of SGS motions and need to be modelled to close the above system of governing equations.

2.1. SGS stress models

Two dynamic SGS stress models are tested in this research, namely, the conventional DM of Lilly [14] and DNM of Wang and Bergstrom [22]. The following text briefly summarizes these two dynamic models.

2.1.1. SGS stress model 1 (DM)

The constitutive relation for the DM is based on a linear tensorial function of the resolved strain rate tensor $\overline{S}_{ij}$, i.e.

$$\tau^*_{ij} = \tau_{ij} - \frac{\tau_{kk}}{3}\delta_{ij} = -2C_S\overline{\Delta}^2|\overline{S}|\overline{S}_{ij}, \tag{4}$$

where $\overline{S}_{ij} \overset{\text{def}}{=} (\partial\bar{u}_i/\partial x_j + \partial\bar{u}_j/\partial x_i)/2$, $|\overline{S}| = (2\overline{S}_{ij}\overline{S}_{ji})^{1/2}$ is the norm of the resolved strain rate tensor, and an asterisk represents a trace-free tensor, i.e.: $(\cdot)^*_{ij} \overset{\text{def}}{=} (\cdot)_{ij} - (\cdot)_{kk}\delta_{ij}/3$. By minimizing the residual of the Germano identity following the dynamic procedure of Lilly [14], the model coefficient C_S is obtained:

$$C_S = -\frac{M_{ij}\mathscr{L}_{ij}}{M_{ij}M_{ij}}, \tag{5}$$

where $\mathscr{L}_{ij} \overset{\text{def}}{=} \widetilde{\bar{u}_i\bar{u}_j} - \tilde{\bar{u}}_i\tilde{\bar{u}}_j$ is the resolved Leonard type stress, and $M_{ij} \overset{\text{def}}{=} \alpha_{ij} - \tilde{\beta}_{ij}$ is a differential tensor, with $\alpha_{ij} \overset{\text{def}}{=} 2\widetilde{\overline{\Delta}}^2|\widetilde{\overline{S}}|\widetilde{\overline{S}}_{ij}$ and $\beta_{ij} \overset{\text{def}}{=} 2\overline{\Delta}^2|\overline{S}|\overline{S}_{ij}$. In the above equations, the filtered quantities at the grid level are denoted using an overbar, while the filtered quantities at the test-grid level for the dynamic procedure are denoted using a tilde. In the present study, instead of using a plane averaging (over the entire statistically homogeneous x_1–x_3 plane) which smears the local characteristic of the model, a local bounding is applied to the coefficient of the DM. First, we bound the calculated coefficient of the DM by $-0.2 \leqslant C_S \leqslant 0.2$ (approximately 92% of the calculated coefficient values fall within this range), and then smooth the coefficient using a 2-D discrete box filter (viz., local plane averaging based on a stencil of 3×3 nodes in the x_1 and x_3 directions).

2.1.2. SGS stress model 2 (DNM)

The second SGS stress model tested is the DNM proposed by Wang and Bergstrom [22], which is based on the explicit quadratic tensorial polynomial constitutive relation originally introduced by Speziale and Gatski [23,24] for the RANS approach, and takes the following form within the context of LES:

$$\tau^*_{ij} = -C_S\beta_{ij} - C_W\gamma_{ij} - C_N\eta_{ij}, \tag{6}$$

where $\gamma_{ij} \overset{\text{def}}{=} 4\overline{\Delta}^2(\overline{S}_{ik}\overline{\Omega}_{kj} + \overline{S}_{jk}\overline{\Omega}_{ki})$, $\eta_{ij} \overset{\text{def}}{=} 4\overline{\Delta}^2(\overline{S}_{ik}\overline{S}_{kj} - \overline{S}_{mn}\overline{S}_{nm}\delta_{ij}/3)$, and δ_{ij} is the Kronecker delta. It can be shown that the optimal values of the three dynamic model coefficients C_S, C_W and C_N can be obtained using the least squares approach as

$$\begin{bmatrix} M_{ij}M_{ij} & M_{ij}W_{ij} & M_{ij}N_{ij} \\ W_{ij}M_{ij} & W_{ij}W_{ij} & W_{ij}N_{ij} \\ N_{ij}M_{ij} & N_{ij}W_{ij} & N_{ij}N_{ij} \end{bmatrix} \cdot \begin{bmatrix} C_S \\ C_W \\ C_N \end{bmatrix} = - \begin{bmatrix} \mathscr{L}^*_{ij}M_{ij} \\ \mathscr{L}^*_{ij}W_{ij} \\ \mathscr{L}^*_{ij}N_{ij} \end{bmatrix}. \tag{7}$$

Analogous to the previous definition of M_{ij}, W_{ij} and N_{ij} are two differential tensors defined as $W_{ij} \overset{\text{def}}{=} \lambda_{ij} - \tilde{\gamma}_{ij}$ and $N_{ij} \overset{\text{def}}{=} \zeta_{ij} - \tilde{\eta}_{ij}$, respectively; with $\lambda_{ij} \overset{\text{def}}{=} 4\widetilde{\overline{\Delta}}^2(\widetilde{\overline{S}}_{ik}\widetilde{\overline{\Omega}}_{kj} + \widetilde{\overline{S}}_{jk}\widetilde{\overline{\Omega}}_{ki})$ and $\zeta_{ij} \overset{\text{def}}{=} 4\widetilde{\overline{\Delta}}^2(\widetilde{\overline{S}}_{ik}\widetilde{\overline{S}}_{kj} - \widetilde{\overline{S}}_{mn}\widetilde{\overline{S}}_{nm}\delta_{ij}/3)$. The design of the modelling constitutive relation [i.e., Eq. (6)], in terms of the choice of the three constituent tensorial base components (i.e., β_{ij}, γ_{ij} and η_{ij}), is not arbitrary: (i) the first term β_{ij} is the well-known Smagorinsky component which primarily relates to the SGS dissipation and forward scatter of TKE from the resolved to subgrid scale motions; (ii) the second term γ_{ij} does not make any contribution to the TKE transfer between the resolved and subgrid scales,

but according to a recent systematic *a priori* LES study of Horiuti [47], it significantly improves the correlation between the exact τ_{ij} extracted from a DNS database and that predicted by the nonlinear model; and (iii) as demonstrated previously [22], the third term η_{ij} contributes significantly to backscatter of TKE from the subgrid to the resolved scales of motion. As such, the constitutive relation represented by Eq. (6) can be understood as a generalization of the conventional DM of Lilly [14] from a linear to a quadratic nonlinear form based on an explicit tensorial polynomial expansion. The three features mentioned above, namely, adequate SGS dissipation level, a high correlation coefficient between the modelled and exact SGS stress in an *a priori* LES test, and realistic reflection of TKE backscatter, are among the most important criteria for evaluation of a successful SGS stress model. The Speziale–Gatski constitutive relation on which the DNM is based offers an effective representation of the three independent terms required to model individually these three important physical features. Due to its nonlinear characteristics, the DNM is numerically robust and can be applied locally without the need for plane averaging in the simulation, which contrasts sharply with the performance of the DM. However, in terms of the efficiency, it is found that the DNM is approximately 25% more computationally expensive than the DM [22].

2.2. SGS heat flux models

Two dynamic SGS HF models are implemented in the simulation, namely, the DEDM-HF introduced by Moin et al. [26], and the DTDM-HF recently proposed by Peng and Davidson [44]. We summarize these two modelling formulae in the following context.

2.2.1. SGS HF model 1 (DEDM-HF)

As mentioned in the previous section, the DEDM-HF is based on the concept of a linear eddy thermal diffusivity in analogy to Fourier's law. In the literature, this model is still the most popular for LES of scalar transport processes. The DEDM-HF adopts the following constitutive relation for modelling the SGS HF vector:

$$h_j = -\alpha_{\text{sgs}}\frac{\partial\bar{\theta}}{\partial x_j} = -\frac{\nu_{\text{sgs}}}{\sigma_{\text{sgs}}}\frac{\partial\bar{\theta}}{\partial x_j} = -\frac{C_S}{\sigma_{\text{sgs}}}\overline{\Delta}^2|\overline{S}|\frac{\partial\bar{\theta}}{\partial x_j}, \tag{8}$$

where α_{sgs} is the SGS eddy thermal diffusivity, σ_{sgs} is SGS Prandtl number set to be 0.5, and C_S is the dynamic model coefficient of the DM.

2.2.2. SGS HF Model 2 (DTDM-HF)

On noting the limitation of the DEDM-HF, Peng and Davidson [44] proposed a novel DTDM-HF based on the concept of a dynamic tensor thermal diffusivity, which no longer relies on the analogy of molecular diffusion and allows for non-alignment between the SGS HF vector and negative resolved temperature gradient vector.[2] The constitutive relation for the DTDM-HF of Peng and Davidson [44] at the grid level takes the following form:

$$h_j = -C_\theta^T\overline{\Delta}^2\overline{S}_{jk}\frac{\partial\bar{\theta}}{\partial x_k}, \tag{9}$$

where C_θ^{T} is the model coefficient and the tensor diffusivity is based on the resolved strain rate tensor, viz. $D_{jk} = C_\theta^{\text{T}}\overline{\Delta}^2\overline{S}_{jk}$. For the dynamic procedure, the test-grid level SGS HF vector is modelled as

$$H_j = -C_\theta^T\widetilde{\overline{\Delta}}^2\widetilde{\overline{S}}_{jk}\frac{\partial\tilde{\bar{\theta}}}{\partial x_k}. \tag{10}$$

Following the dynamic modelling approach of Germano et al. [13], a similar vector identity exists to relate h_j to H_j, viz.

$$\mathscr{L}_j = H_j - \tilde{h}_j, \tag{11}$$

where $\mathscr{L}_j \overset{\text{def}}{=} \widetilde{\bar{u}_j\bar{\theta}} - \tilde{\bar{u}}_j\tilde{\bar{\theta}}$. By minimizing the norm of the residual vector of Eq. (11) using the least squares method and assuming that $\widetilde{C_\theta^{\text{T}}b_j} \approx C_\theta^{\text{T}}\tilde{b}_j$, the dynamic coefficient for the DTDM-HF is obtained, viz.

$$C_\theta^{\text{T}} = -\frac{\mathscr{L}_j M_j}{M_j M_j}, \tag{12}$$

where $M_j \overset{\text{def}}{=} a_j - \tilde{b}_j$ with the base vectors defined as

$$b_j = \overline{\Delta}^2\overline{S}_{jk}\frac{\partial\bar{\theta}}{\partial x_k} \quad \text{and} \quad a_j = \widetilde{\overline{\Delta}}^2\widetilde{\overline{S}}_{jk}\frac{\partial\tilde{\bar{\theta}}}{\partial x_k}. \tag{13}$$

Unlike the DEDM-HF [cf. Eq. (8)], the DTDM-HF of Peng and Davidson [44] [cf. Eq. (9)] does not require the SGS heat flux be aligned with the negative resolved temperature gradient vector, instead, it modifies the heat flux vector h_j in response to both the resolved strain rate tensor and temperature gradient in all three coordinate directions through the contraction between $\overline{S}_{jk}$ and $\partial\bar{\theta}/\partial x_k$. As such, in theory, the SGS heat flux component in a direction with zero mean temperature gradient can still be non-trivial due to the temperature gradients present in the other two directions.

[2] In the original paper of Peng and Davidson [44], the DTDM-HF is referred to as a "dynamic nonlinear tensor diffusivity SGS heat flux model". It is considered as nonlinear only in the sense that the direction of h_j is no longer required to be parallel to $-\partial\bar{\theta}/\partial x_j$ (owing to the effect of tensor contraction between $\overline{S}_{jk}$ and $\partial\bar{\theta}/\partial x_k$), which is in sharp contrast to the behaviour of the linear eddy thermal diffusivity model (viz., DEDM-HF). However, it should be indicated that the tensor diffusivity of the DTDM-HF is, strictly speaking, a *homogeneous linear* tensor function of $\overline{S}_{jk}$, i.e. $D_{jk} = f(\overline{S}_{jk}) = C_\theta^{\text{T}}\overline{\Delta}^2\overline{S}_{jk}$. Here, *homogeneity* derives from the terminology of linear algebra, which refers to a linear transformation that obeys: $D_{jk} = f(\overline{S}_{jk}) = \mathbf{0}$ if $\overline{S}_{jk} = \mathbf{0}$. Noting the difference above, the DTDM-HF Peng and Davidson is also referred to, in a more strict sense, as the "dynamic homogeneous linear tensor diffusivity model for representing the SGS heat flux (DHLTDM-HF) based on the resolved strain rate tensor and temperature gradient" by Wang et al. [12].

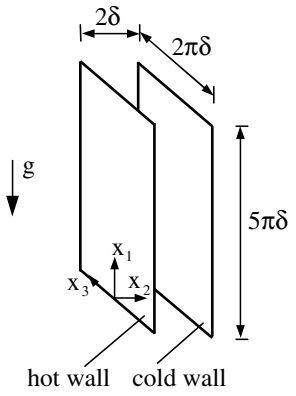

Fig. 1. Illustration of the physical domain of the combined forced and natural convective channel flow.

3. Physical model and numerical method

The physical model tested in this research is a combined forced and natural convection (or, mixed convention) between two vertical parallel plates maintained at two different temperatures. Specifically, we consider a benchmark test case of Kasagi and Nishimura [6] and compare the obtained LES results with the reported DNS results [6,45,46]. The physical domain of the test flow is described in Fig. 1. The flow is characterized by a Grashof number of $Gr = 9.6 \times 10^5$ and a Reynolds number of $Re_\tau^a = 150$ (determined by the mean driving pressure gradient in the streamwise direction). Here, $Re_\tau^a \overset{\text{def}}{=} u_\tau^a \delta / \nu$ and u_τ^a is the average value of the friction velocities at the two walls. So, $Re_\tau^a = (Re_{\tau h} + Re_{\tau c})/2$. The pressure gradient drives the mean flow upward, while the buoyant force acts in the upward (aiding flow) and downward (opposing flow) directions near the hot and cold walls, respectively. Compared with the forced convection case ($Gr = 0$), the mean velocity profile for mixed convection becomes increasingly asymmetric as the Grashof number increases [6,46,3]. In general, the turbulent transport is enhanced in the opposing flow region and is suppressed in the aiding flow region. As mentioned in Davidson et al. [46], because the velocity profile is asymmetric in the wall-normal direction, the value of the friction velocity τ_w (and therefore, the Reynolds number Re_τ) at the hot wall is different than that at the cold wall, i.e. $\tau_{wh} \neq \tau_{wc}$ (and $Re_{\tau h} \neq Re_{\tau c}$). As such, due to the buoyancy effect, it is expected that the value of Re_τ^a obtained from simulation deviates from the nominal value of 150, and we will revisit this subject later when discussing Table 1.

The governing equations are discretized using the finite volume method. Following the approach of Kim and Moin [48], the momentum equations were solved using a fractional-step method where the nonlinear term was discretized using a second-order explicit Adams–Bashforth scheme and the viscous diffusion term was discretized using a second-order Crank–Nicolson scheme. A second-order central difference scheme was applied on a collocated grid for spatial discretization. At each time step, the pressure field was updated using an pressure correction method and the Poisson type pressure correction equation was solved using a multi-grid method. The check-board effect associated with the adopted collocated grid system was removed using a momentum interpolation scheme for evaluating the face value of the velocity [49]. To solve the filtered thermal energy equation, a fourth-order Runge–Kutta method was used to advance the temperature field over a single time step. The time period used to obtain the turbulent statistics was 10,000 time steps after the flow becomes fully developed. In order to extract the value of a filtered variable at the test-grid level to perform the dynamic modelling procedure, the boundary thermal-fluid fields were processed using a second-order Gaussian filter and the interior fields were processed using a fourth-order discrete Gaussian filter. For the formulation of these discrete filters, the reader is referred to Sagaut and Grohens [50].

No-slip and no-penetration boundary conditions were imposed on the velocity components at the walls, while the temperatures on the two side walls were set to fixed values derived from the given Grashof number. Periodic boundary conditions were imposed in the streamwise and spanwise directions. The computational domain was set to be $5\pi\delta \times 2\delta \times 2\pi\delta$, and $48 \times 32 \times 48$ control volumes were used for discretizing the domain in the streamwise (x_1), wall-normal (x_2) and spanwise (x_3) directions, respectively. The grid is uniform in the streamwise and spanwise directions and is refined in the wall-normal direction using a hyperbolic-tangent function, such that the first interior node off the wall is located at $x_2^+ \approx 1.2$. Since in an LES approach, not all scales of motion are resolved, the number of the control volumes to be employed is less than that used in a DNS approach. For instance, for a similar test case ($Gr = 7.68 \times 10^6$ and $Re_\tau^a = 150$), Davidson et al. [46] used $128 \times 96 \times 96$ control volumes in their DNS study of mixed convection. In the absence of filtered DNS data, the value of the resolved scale variables obtained from the simulation will be compared directly with the DNS

Table 1
Physical quantities of the flow

	Re_τ^a	Re_b	$\frac{Gr}{Re_b^2}$	u_τ		$C_f \times 10^{-3}$		Nu	
				Hot	Cold	Hot	Cold	Hot	Cold
DNS [6]	150	4494	0.0475	–	–	9.90	7.90	7.4	20.9
DM and DEDM-HF	145	4270	0.0526	0.0565	0.0522	9.59	7.96	7.11	21.6
DNM and DTDM-HF	147	4380	0.0500	0.0568	0.0535	9.55	7.98	7.32	21.4

results. All quantities denoted by $\langle \cdot \rangle$ are averaged both in time and over homogeneous planes. In presenting the results, quantities non-dimensionalized using the wall friction velocity u_τ and friction temperature T_τ are denoted with a superscript "+".

4. Result analysis

Table 1 summarizes the flow conditions and some important parameters that characterize thermal-fluid flow fields obtained from the LES and DNS approaches. Although slight differences exist, Table 1 indicates that the LES predictions of those characteristic flow parameters (such as the Reynolds number, and resolved wall friction coefficient and Nusselt number) based on both sets of linear and nonlinear models are, in general, consistent with the reported DNS data. The Reynolds numbers (Re_τ^a and Re_b) calculated from the LES are slightly smaller than those from the DNS performed by Kasagi and Nishimura [6], with a difference less than 5%. The value of the resolved friction coefficient predicted using both the LES and DNS is larger at the hot wall and smaller at the cold wall. In contrast, the predicted value of the Nusselt number is smaller in the hot wall region and larger in the cold wall region. The reason that the value of the resolved wall friction coefficient increases at the hot wall and decreases at the cold wall, is due to the fact that buoyancy aids the upstream flow motion (consistent with the effect caused by the mean streamwise driving pressure gradient) near the hot wall while opposing it near the cold wall. The Nusselt number in both the hot and cold wall regions is defined as the ratio of the actual heat transferred through the wall to the heat transfer that would occur through conduction [6], viz. $Nu = 2q_w/[\lambda(\theta_D - \theta_w)/D]$. Here, q_w represents the wall heat flux, θ_w is the wall temperature, D is the distance measured from the wall to the maximum streamwise velocity location, and $\theta_D \overset{\text{def}}{=} \int_0^D \langle\bar{\theta}\rangle \, dx_2/D$ is the bulk averaged temperature over the special distance D. Owing to the deformation of the mean velocity profile (see Fig. 2a), the value of D for the hot wall region is smaller than that for the cold wall region. As such, the fluid heat conduction [i.e., $\lambda(\theta_D - \theta_w)/D$] near the hot wall is larger than that near the cold wall. Given the definition of the Nusselt number and the condition that the averaged value of q_w from the two walls must be equal to satisfy conservation of energy, the Nusselt number in the hot wall region is smaller than that in the cold wall region. These observations are in agreement with the previous investigations conducted by other researchers [3,6,46].

4.1. Mean resolved temperature and velocity profiles

Fig. 2a and b shows the profiles of the mean resolved streamwise velocity and temperature across the channel for the mixed convective flow ($Gr = 9.6 \times 10^5$ and $Re_\tau^a = 150$). The DNS data of Kasagi and Nishimura [6] and Kuroda et al. [45] are used for validating the LES

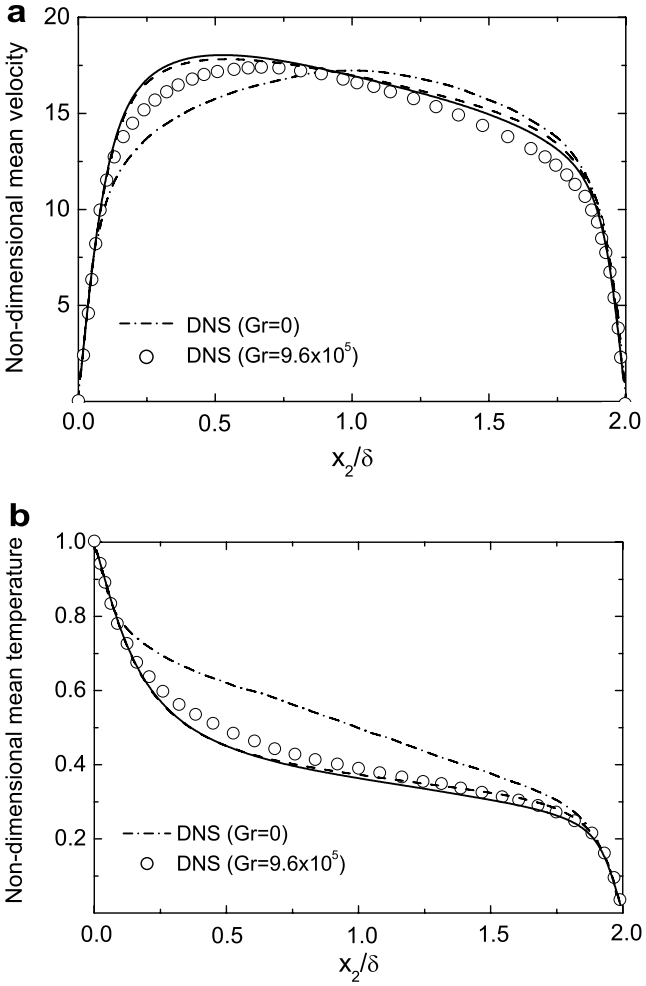

Fig. 2. Mean resolved velocity and temperature profiles across the channel: (a) non-dimensional mean streamwise velocity $\langle \bar{u}_1 \rangle / u_\tau^a$; (b) non-dimensional mean temperature $\frac{\langle\bar{\theta}\rangle - \theta_{wc}}{\theta_{wh} - \theta_{wc}}$. Solid line: DM and DEDM-HF; dash line: DNM and DTDM-HF. DNS results in Fig. 2a: mixed convection ($Gr = 9.6 \times 10^5$ and $Re_\tau^a = 150$) refers to Kasagi and Nishimura [6]; forced convection ($Gr = 0$ and $Re_\tau = 150$) refers to Kuroda et al. [45]. DNS results in Fig. 2b: both forced and mixed convection cases refer to Kasagi and Nishimura [6].

results. The mean velocity and temperature profiles are symmetric for the forced convection case whereas asymmetric for the mixed convection case. Compared with the DNS data [6], the results predicted by both sets of linear and nonlinear models are very similar: near the hot wall (or, in the aiding flow region), the mean velocity is slightly overpredicted and mean temperature is slightly underpredicted. From Fig. 2b, it is observed that the mean temperature profile near the cold wall (or, in the opposing flow region) predicted by the set of nonlinear models agrees better with the DNS result than that predicted by the set of linear models.

Fig. 3a and b shows the mean velocity and temperature using wall coordinates. We use the suffixes _h and _c to denote quantities related to the hot and cold walls, respectively. Compared with the forced convection case ($Gr = 0$ and $Re_\tau = 150$) of Kuroda et al. [45], the mean resolved velocity profile for mixed convection deviates from the

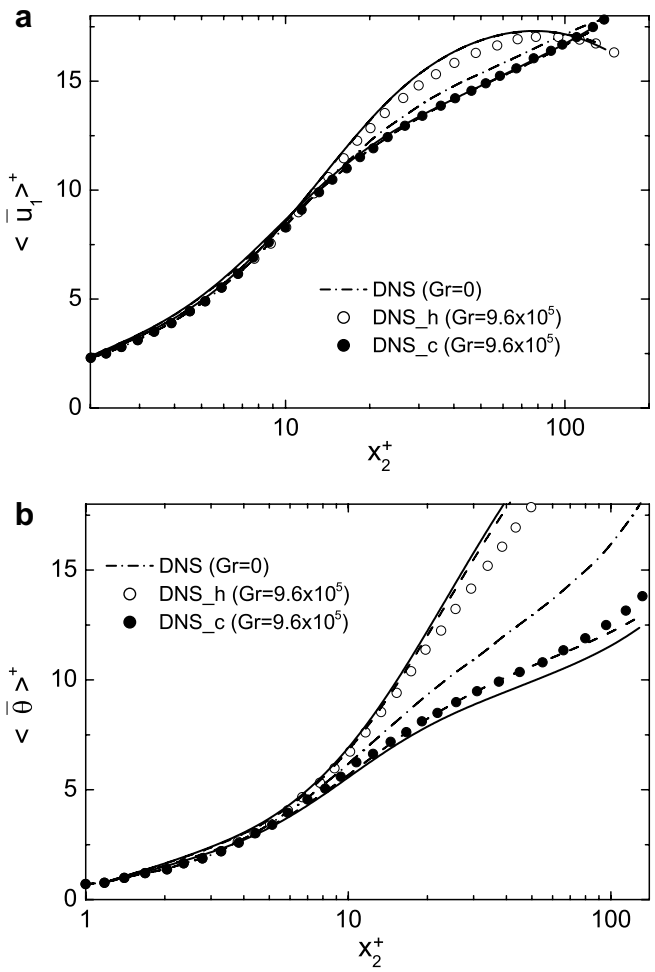

Fig. 3. Mean resolved velocity and temperature profiles across the channel displayed using wall coordinates: (a) velocity; (b) temperature. Solid line: DM and DEDM-HF; dash line: DNM and DTDM-HF. DNS results in Fig. 3a: mixed convection ($Gr = 9.6 \times 10^5$ and $Re_\tau^a = 150$) refers to Kasagi and Nishimura [6]; forced convection ($Gr = 0$ and $Re_\tau = 150$) refers to Kuroda et al. [45]. DNS results in Fig. 3b: both forced and mixed convection cases refer to Kasagi and Nishimura [6].

conventional logarithmic law in response to the buoyant force: the velocity shifts slightly downward near the cold wall, whereas it becomes curved and shifts upward near the hot wall. The mean resolved temperature profile also deviates from the profile of forced convection: it shifts downward and upward near the cold and hot walls, respectively. Although both sets of linear and nonlinear SGS models yield almost the same prediction for the mean resolved velocity [cf. Fig. 3a], it appears that the mean resolved temperature profile predicted by the set of nonlinear SGS models is closer to the DNS result [6] than that predicted by the set of linear SGS models, especially in the cold wall region [cf. Fig. 3b].

4.2. Resolved shear stresses and heat fluxes

To illustrate the basic characteristics of the flow in an intuitive manner, we show in Fig. 4 the instantaneous

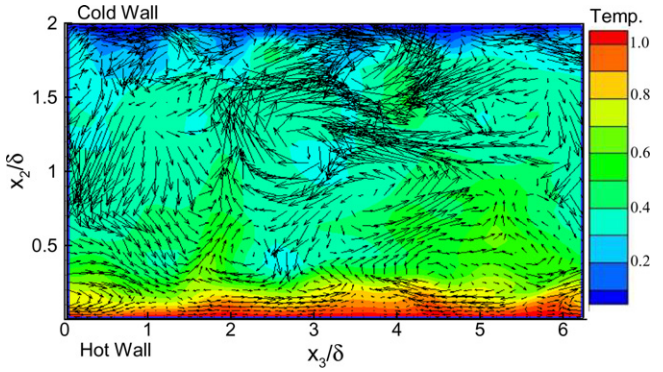

Fig. 4. Instantaneous velocity vectors and temperature contour in a central transverse plane predicted by the set of dynamic nonlinear SGS models ($Gr = 9.6 \times 10^5$ and $Re_\tau^a = 150$). The temperature is non-dimensionalized as $\frac{\langle\bar{\theta}\rangle - \theta_{wc}}{\theta_{wh} - \theta_{wc}}$.

velocity and temperature fields in the central transverse plane obtained using the set of nonlinear SGS models. From the figure, it is observed that the flow structures indicated by both the temperature contours and instantaneous velocity vectors near the cold wall are larger and more intense than those near the hot wall. This is because buoyancy aids the upstream flow motion in the region near the hot wall and opposes the upstream flow motion in the region near the cold wall with the consequent suppression and enhancement of turbulence in these two regions, respectively. To investigate the effects of buoyancy on the balance and momentum and thermal energy, we decompose the instantaneous filtered quantity into the mean and residual components:

$$\bar{\phi} = \langle\bar{\phi}\rangle + \bar{\phi}'', \tag{14}$$

where $\langle\bar{\phi}\rangle$ denotes a filtered quantity averaged both in time and over the $x_1 - x_3$ plane, and $\bar{\phi}''$ denotes the residual component relative to $\langle\bar{\phi}\rangle$. By substituting Eq. (14) into the filtered streamwise momentum equation and then integrating the resulting equation from $x_2 = 0$ to x_2, the equation which balances the time- and plane-averaged shear stresses at an arbitrary wall-normal location x_2 is obtained

$$\nu\frac{\partial\langle\bar{u}_1\rangle}{\partial x_2} - \langle\bar{u}_1''\bar{u}_2''\rangle + \int_0^{x_2}\beta g(\langle\bar{\theta}\rangle - \Theta_r)\,dx_2 - \langle\tau_{12}\rangle = \frac{1}{\rho}\frac{\partial\langle\bar{p}\rangle}{\partial x_1}x_2 + \frac{\tau_{wh}}{\rho}. \tag{15}$$

In order to derive the above approximate equation, two additional assumptions need to be made: the flow is (i) statistically stationary and (ii) homogeneous in the $x_1 - x_3$ plane. The four terms on the left-hand side (LHS) of Eq. (15) represent the resolved viscous shear stress, resolved Reynolds (or, turbulent) shear stress, resolved buoyant shear stress, and SGS shear stress, respectively. The two terms on the right-hand side (RHS) of the equation represent the resolved integrated driving force due to the mean streamwise pressure gradient, and the resolved viscous shear stress at the hot wall, respectively.

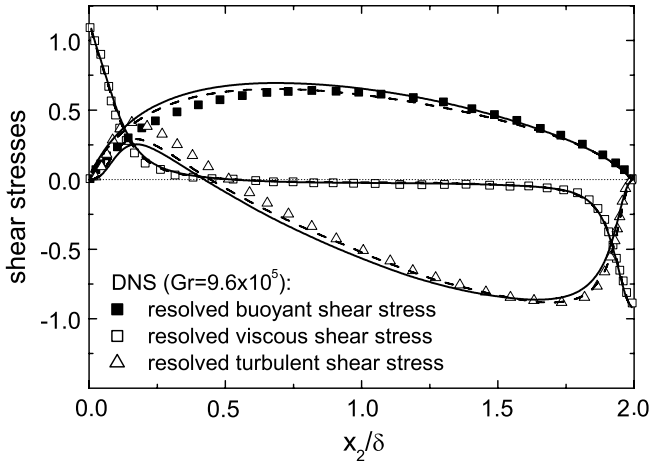

Fig. 5. Non-dimensional shear stresses predicted by the two sets of linear and nonlinear SGS models. Solid line: DM and DEDM-HF; dash line: DNM and DTDM-HF. DNS results ($Gr = 9.6 \times 10^5$ and $Re_\tau^a = 150$) refer to Kasagi and Nishimura [6].

The profiles of the first three terms on the LHS of Eq. (15), normalized by the value of the viscous shear stress term averaged over both walls [i.e., $\tau_w^a/\rho = (u_\tau^a)^2$], are shown in Fig. 5 in comparison with the DNS results of Kasagi and Nishimura [6]. Since the SGS shear stress component $-\langle\tau_{12}\rangle$ is an order smaller than these three terms, we will separately analyze this SGS effect in Section 4.4. In order for Eq. (15) to balance at both wall surfaces, the reference temperature Θ_r is taken as the bulk temperature, viz. $\Theta_r = \theta_b = \int_0^{2\delta}\langle\bar{\theta}\rangle\,dx_2/(2\delta)$. With this convention, the resolved buoyant shear stress term in Eq. (15) vanishes at both wall surfaces. From Fig. 5, it is observed that the LES prediction of the resolved viscous shear stress using both the linear and nonlinear sets of models is in good agreement with the DNS result [6]. However, the resolved buoyant shear stress is slightly overpredicted near the hot wall, and in contrast, the resolved Reynolds shear stress $-\langle\bar{u}_1''\bar{u}_2''\rangle$ is underpredicted in the same region. Fig. 6 shows the absolute value of the resolved Reynolds shear stress using wall coordinates. From the figure, it is observed that due to the effect of buoyancy, $|\langle\bar{u}_1''\bar{u}_2''\rangle^+|$ is enhanced near the cold wall and suppressed near the hot wall. The LES results predicted by both sets of models agree better with the DNS result in the cold wall region than in the hot wall region. Furthermore, near the cold wall, the set of nonlinear models yields a prediction of $|\langle\bar{u}_1''\bar{u}_2''\rangle^+|$ closer to the DNS data than that predicted by the set of linear models.

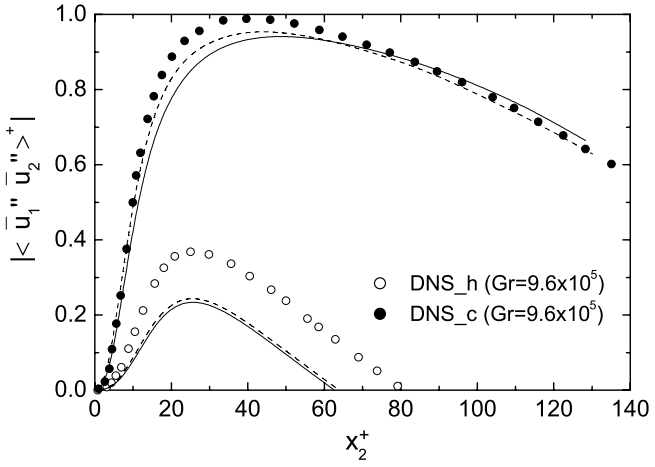

Fig. 6. Resolved Reynolds shear stress displayed using wall coordinates. Solid line: DM and DEDM-HF; dash line: DNM and DTDM-HF. DNS results ($Gr = 9.6 \times 10^5$ and $Re_\tau^a = 150$) refer to Kasagi and Nishimura [6].

Following a similar procedure to derive Eq. (15), the time- and plane-averaged equation that balances the mean wall-normal heat fluxes at any arbitrary wall-normal location x_2 can be obtained from the filtered energy equation (3):

$$-\alpha\frac{\partial\langle\bar{\theta}\rangle}{\partial x_2} + \langle\bar{u}_2''\bar{\theta}''\rangle + \langle h_2\rangle = \frac{q_{wh}}{\rho c_P}, \tag{16}$$

where $q_{wh} \overset{def}{=} -\lambda\frac{\partial\langle\bar{\theta}\rangle}{\partial x_2}|_{x_2=0}$ is the resolved molecular heat flux at the hot wall, and the three terms on the LHS of Eq. (16) correspond to the resolved molecular heat flux, resolved turbulent heat flux, and SGS wall-normal heat flux, respectively. Fig. 7 plots the resolved molecular and turbulent heat fluxes, which are normalized using the molecular heat flux at the hot wall $q_{wh}/(\rho c_P) = u_{\tau h}T_{\tau h}$ (we will discuss the SGS heat fluxes $\langle h_1\rangle$ and $\langle h_2\rangle$ separately in Section 4.4). As shown in the figure, in comparison with the molecular heat flux profile of the forced convection case ($Gr = 0$ and $Re_\tau = 150$, based on DNS study of Davidson et al. [46]), the molecular heat flux of the mixed convection case predicted by both the current LES ($Gr = 9.6 \times 10^5$ and $Re_\tau^a = 150$) and DNS ($Gr = 7.68 \times 10^6$ and $Re_\tau^a = 150$) by Davidson et al. [46] increases noticeably near the hot wall, and decreases slightly near the cold wall; in contrast, the profile of the resolved turbulent heat flux displays the

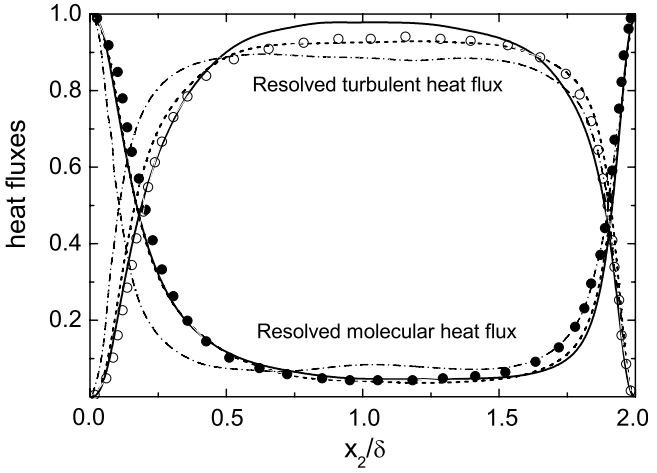

Fig. 7. Non-dimensional wall-normal heat fluxes predicted by the two sets of linear and nonlinear SGS models ($Gr = 9.6 \times 10^5$ and $Re_\tau^a = 150$). Solid line: DM and DEDM-HF; dash line: DNM and DTDM-HF. Dash dot line: DNS ($Gr = 0$, Davidson et al. [46]); symbols (● and ○): DNS ($Gr = 7.68 \times 10^6$, Davidson et al. [46]).

opposite trend. This is consistent with the notion that the turbulent motions are enhanced near the cold wall and suppressed near the hot wall. Also shown in the figure, the profiles of the resolved molecular heat flux predicted by both sets of the models are very similar; in contrast, the profiles of the resolved turbulent heat flux predicted by these two sets of models are notably different.

Fig. 8 shows the resolved streamwise and wall-normal turbulent heat fluxes using the wall coordinate (i.e., $\langle \bar{u}_1'' \bar{\theta}'' \rangle^+$ and $\langle \bar{u}_2'' \bar{\theta}'' \rangle^+$, respectively). Both sets of linear and nonlinear models capture the trend of the DNS profile. Theoretically speaking, for a thermal convective flow in a plane channel, the time- and plane-averaged heat flux obtained from a DNS approach can be approximately recovered by an LES approach using the time- and plane-averaged resolved and SGS heat fluxes. However, because the resolved heat flux is an important physical quantity and its value usually dominates the SGS heat flux contribution in LES of many engineering and theoretical test flows, it is still popular to directly compare the resolved heat flux with the DNS results in literature. This direct comparison can be useful especially in a comparative study of different SGS modelling approaches. If the test condition is the same, the SGS modelling approach which produces results that are in better conformance with the DNS data can be considered as a more desirable approach. As shown in Fig. 8a, in the cold wall region, the set of nonlinear models overpredicts the peak value of the streamwise turbulent heat flux $\langle \bar{u}_1'' \bar{\theta}'' \rangle^+$ in comparison with the DNS data [6]; in contrast, the set of linear SGS models underpredicts the peak value. From Fig. 8b, it is observed that the prediction of the wall-normal turbulent heat flux in both the hot and cold wall regions by the set of nonlinear SGS models is generally in better conformance with the DNS data [6] than that predicted by the set of linear SGS models. Fig. 9 re-plots the profiles of the resolved streamwise and wall-normal turbulent heat fluxes using logarithmic coordinates based on the same data set for Fig. 8. Following Na and Hanratty [51], it can be shown using Taylor series expansion that in the vicinity of the wall, the following relations hold: $\langle \bar{u}_1'' \bar{\theta}'' \rangle^+ \propto x_2^{+2}$ and $\langle \bar{u}_2'' \bar{\theta}'' \rangle^+ \propto x_2^{+3}$. Such near-wall restrictions are evident in Fig. 9a and b, and valid in both the hot and cold wall regions.

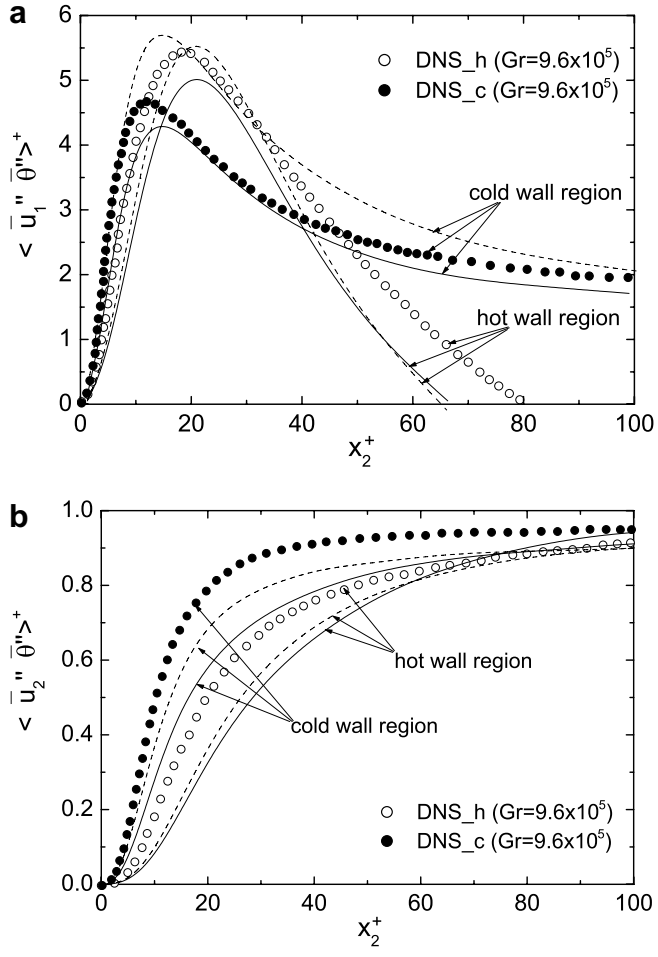

Fig. 8. Resolved turbulent heat fluxes displayed using wall coordinates: (a) streamwise; (b) wall-normal. Solid line: DM and DEDM-HF; dash line: DNM and DTDM-HF. DNS results ($Gr = 9.6 \times 10^5$ and $Re_\tau^a = 150$) refer to Kasagi and Nishimura [6].

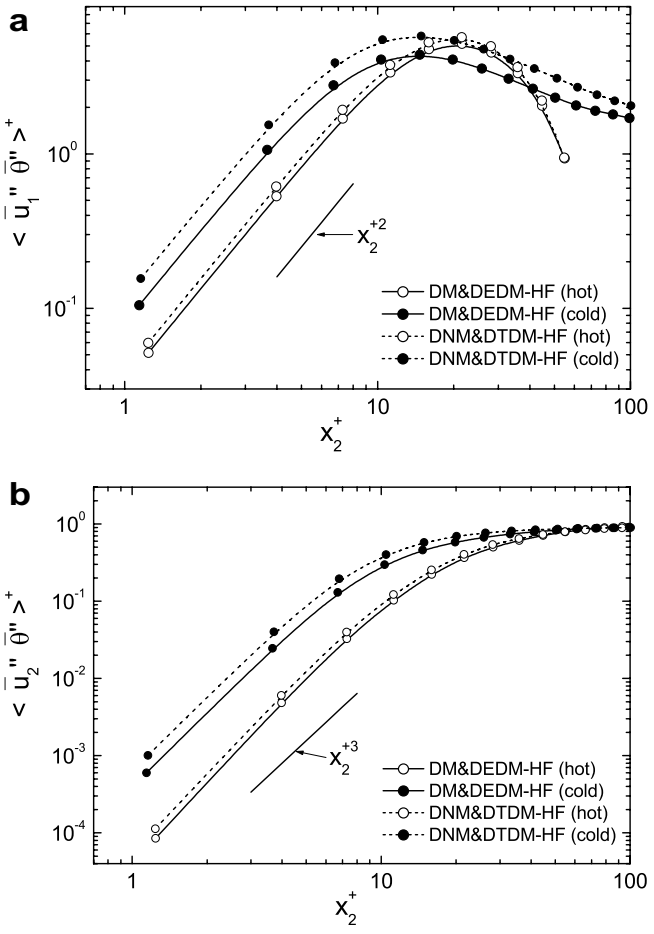

Fig. 9. Resolved turbulent heat fluxes displayed using logarithmic wall coordinates ($Gr = 9.6 \times 10^5$ and $Re_\tau^a = 150$): (a) streamwise component; (b) wall-normal component.

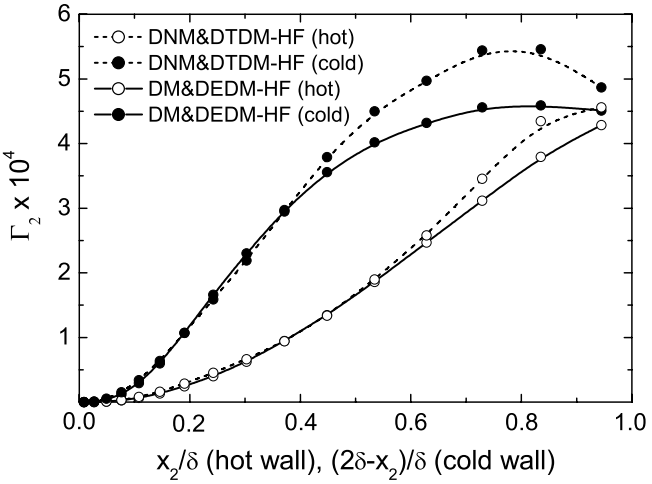

Fig. 10. Effective eddy thermal diffusivity for the wall-normal turbulent heat flux ($Gr = 9.6 \times 10^5$ and $Re_\tau^a = 150$).

The effective eddy thermal diffusivity for the wall-normal turbulent heat flux is defined as $\Gamma_2 = -\langle \bar{u}_2'' \bar{\theta}'' \rangle / (d\langle \bar{\theta} \rangle / \mathrm{d}x_2)$. Fig. 10 compares the value of Γ_2 predicted by the two sets of linear and nonlinear SGS models. Common to both sets of SGS models, the predicted level of Γ_2 near the cold wall is larger than that near the hot wall. This is due to the fact that buoyancy enhances and suppresses the turbulence heat fluxes near the cold and hot walls, respectively [cf. Fig. 8b]. As shown in Fig. 10, the value of Γ_2 predicted using the set of nonlinear models is noticeably larger than that predicted using the set of linear SGS models, especially in the central region of the channel.

4.3. Velocity and temperature fluctuations

For the forced convective flow with $Gr = 0$, the variance of the resolved temperature and velocity field (corresponding to resolved turbulence intensities for the latter case) is distributed in a symmetrical manner across the channel. However, for the mixed convection case of $Gr > 0$, the values of the resolved turbulence intensities near the hot and cold walls are expected to be different due to the existence of the buoyant force. Fig. 11 shows that the effect of buoyancy is to enhance the level of all three velocity fluctuation components (represented by $\bar{u}^+_{1,\mathrm{rms}}, \bar{u}^+_{2,\mathrm{rms}}$ and $\bar{u}^+_{3,\mathrm{rms}}$, respectively) near the cold wall, and to reduce it near the hot wall. Here, the resolved velocity fluctuations are evaluated using the non-dimensionalized root-mean-square values defined as $\bar{u}^+_{i,\mathrm{rms}} \overset{\mathrm{def}}{=} \langle (\frac{\bar{u}_i - \langle \bar{u}_i \rangle}{u_\tau})^2 \rangle^{1/2}$ for $i = 1$, 2 and 3. From Fig. 11, it is observed that the predictions from both sets of linear and nonlinear models in general agree with of the reported DNS results of Kasagi and Nishimura [6]. However, as indicated by Fig. 11a, the set of nonlinear models yields a slightly better prediction of the streamwise velocity fluctuation $\bar{u}^+_{1,\mathrm{rms}}$ in the opposing flow region than the set of linear models.

Fig. 12 compares the resolved temperature fluctuation $\bar{\theta}^+_{\mathrm{rms}} \overset{\mathrm{def}}{=} \langle (\frac{\bar{\theta} - \langle \bar{\theta} \rangle}{T_\tau})^2 \rangle^{1/2}$ predicted using the two sets of SGS

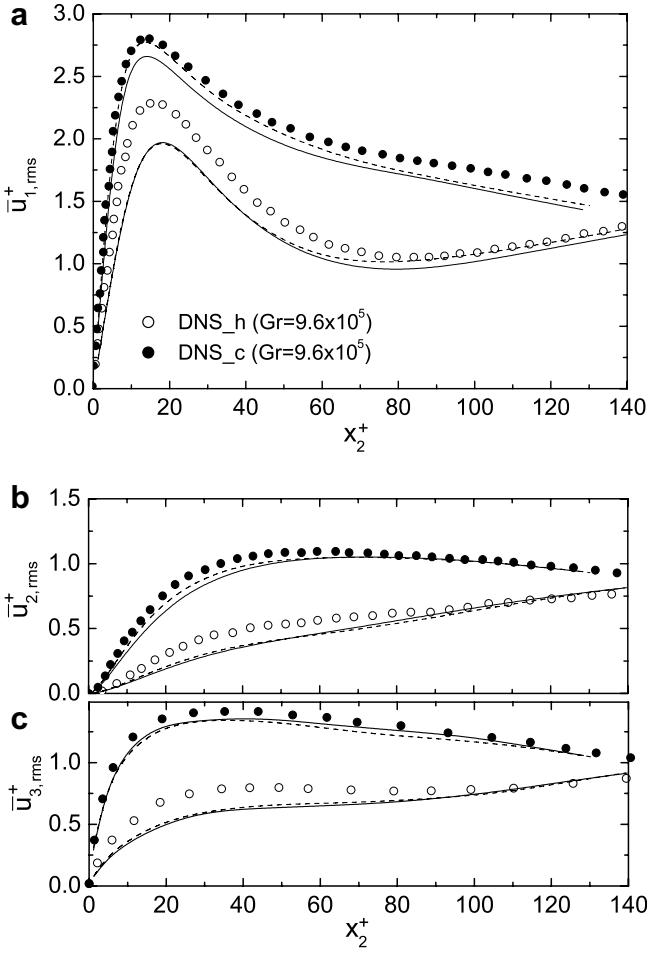

Fig. 11. Resolved velocity fluctuations in wall coordinates: (a) streamwise; (b) wall-normal; (c) spanwise. Solid line: DM and DEDM-HF; dash line: DNM and DTDM-HF. DNS results ($Gr = 9.6 \times 10^5$ and $Re_\tau^a = 150$) refer to Kasagi and Nishimura [6].

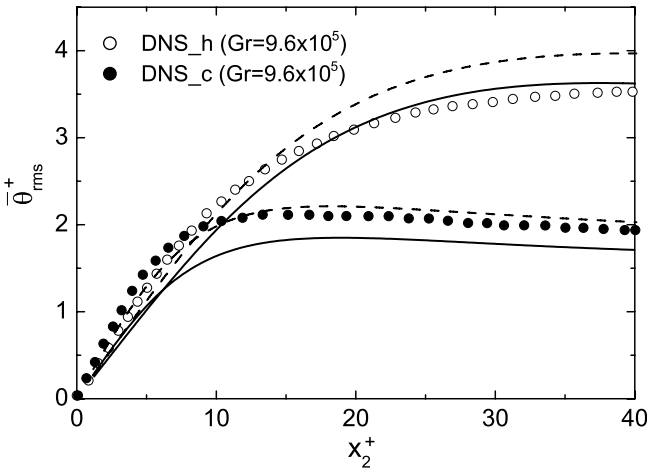

Fig. 12. Resolved temperature fluctuations in wall coordinates. Solid line: DM and DEDM-HF; dash line: DNM and DTDM-HF. DNS results ($Gr = 9.6 \times 10^5$ and $Re_\tau^a = 150$) refer to Kasagi and Nishimura [6].

models with the DNS data [6]. In general, it is observed that the prediction of $\bar{\theta}^+_{\mathrm{rms}}$ from both sets of linear and

nonlinear SGS models is similar to the DNS results. It is interesting to observe that the effect of buoyancy on the resolved temperature fluctuation is exactly the opposite to its effect on the resolved velocity functions as discussed above: $\bar{\theta}^{+}_{\mathrm{rms}}$ is suppressed near the cold wall and enhanced near the hot wall. This result is consistent with the observation Davidson et al. [46] in their DNS study of mixed convection.

4.4. SGS effects

In Sections 4.1–4.3, we have observed that although slight differences exist, some of the mean resolved scale quantities predicted by the two different sets of SGS models are similar in terms their values, e.g. the mean resolved streamwise velocity and temperature shown in Fig. 2 and the mean resolved viscous shear stress shown in Fig. 5. This is not surprising, since in LES the large scale motions which contribute the most to the resolved fields are calculated directly. In order to understand a SGS model in greater detail, refined examination should be based on the statistics related to residual SGS motions, which of course, are expected to be more erratic than the resolved large-scale motions. For this purpose, we demonstrate in Figs. 13 and 14 some SGS effects involved in the current LES study of mixed convection.

Fig. 13 compares the SGS shear stress $-\tau_{12}$ predicted by the two sets of linear and nonlinear SGS models. Although the predictions of both sets of SGS models show similar trends, the SGS shear stress predicted by the set of linear SGS models is higher than that predicted by the set of nonlinear SGS models. Fig. 14 compares the SGS heat fluxes predicted by the two sets of linear and nonlinear SGS models. As shown in the figure, the SGS heat fluxes produced by the two sets of SGS models are markedly different: the set of linear SGS models yields $|\langle h_1\rangle| \leqslant |\langle h_2\rangle|$, whereas the set of nonlinear SGS models yields $|\langle h_1\rangle| \geqslant |\langle h_2\rangle|$. According to Peng and Davidson [44], it is more reasonable to obtain a result of $|\langle h_1\rangle| \geqslant |\langle h_2\rangle|$, which is in line with the observation that the level of the resolved streamwise turbulent heat flux $\langle \bar{u}_1''\bar{\theta}''\rangle$ is usually larger than that of the resolved wall-normal turbulent heat flux $\langle \bar{u}_2''\bar{\theta}''\rangle$. Furthermore, it is noted that the set of nonlinear SGS models enhances the magnitude of $\langle h_1\rangle$, even though no mean temperature gradient exists in the streamwise direction. An explanation for this observation is that in comparison with the DEDM-HF, the DTDM-HF has more degrees of freedom for geometrical representation of the SGS HF vector, and allows for a non-alignment between h_j and $-\partial\bar{\theta}/\partial x_j$ to reflect the physics of turbulent thermal energy transport at the subgrid scale.

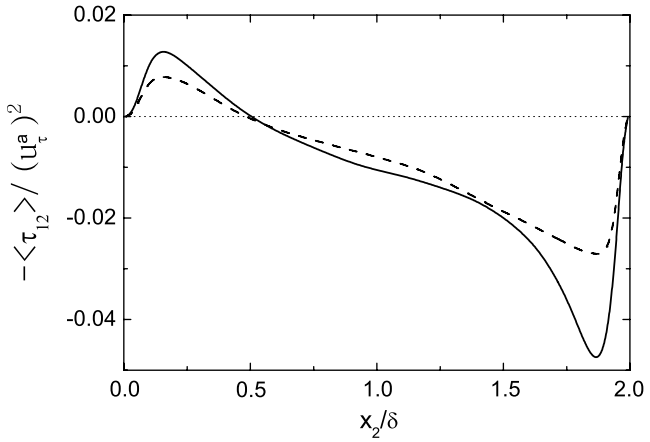

Fig. 13. SGS shear stress produced by SGS models ($Gr = 9.6 \times 10^5$ and $Re_\tau^a = 150$). Solid line: DM and DEDM-HF; dash line: DNM and DTDM-HF.

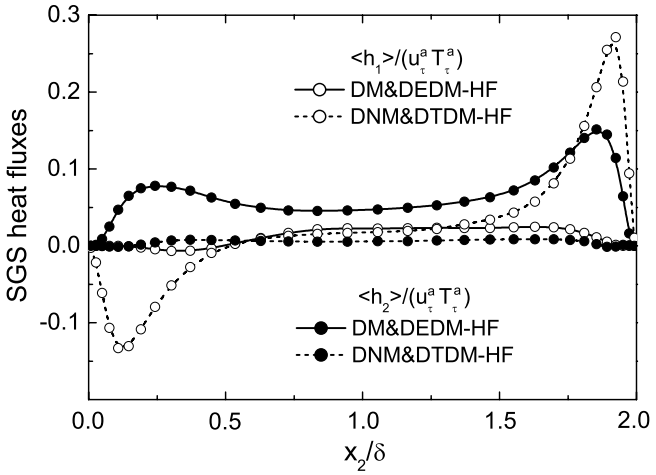

Fig. 14. SGS heat fluxes produced by SGS models ($Gr = 9.6 \times 10^5$ and $Re_\tau^a = 150$).

5. Conclusions

In this research, LES of combined forced and natural convection between two vertical plates has been performed. Prototypical flow features of the resolved temperature and velocity fields, and mean turbulent shear stresses and heat fluxes have been reproduced at the resolved scale and compared with the DNS results. It is observed that in contrast to forced convective flows driven purely by the mean pressure gradient, the existence of buoyancy in the current test case has a significant impact on both the resolved and subgrid-scale quantities. Due to the buoyancy effects, the distribution of many flow parameters is asymmetrical across the channel, which includes the wall-normal distribution of the mean resolved temperature and velocity fields, resolved turbulent and subgrid-scale shear stresses and heat fluxes, root-mean-square value of the fluctuation in the filtered velocity and temperature fields, and effective eddy thermal diffusivity for the resolved turbulent heat flux.

Two sets of dynamic SGS models were tested in the simulation, i.e. the set of linear SGS models with the DM for modelling the SGS stress and the DEDM-HF for modelling the SGS HF, and the set of nonlinear SGS models with the DNM for modelling the SGS stress and the DTDM-HF for modelling the SGS HF. The performances of these two sets of SGS models are different in terms of the SGS motions. In

particular, their predictions for the SGS shear stress and SGS heat fluxes are markedly different. Although notable differences exist between these two sets of SGS models at the subgrid-scale level, it is observed that some flow quantities predicted by these two sets of SGS models are similar at the resolved scale. This is because in an LES approach, large dominant turbulent motions and thermal energy transport processes are directly computed and the contribution from the SGS motions is usually limited. In terms of the time- and plane-averaged values, the SGS shear stress ($-\tau_{12}$) predicted by both sets of SGS models is less than 3% of the resolved Reynolds shear stress; and the wall-normal SGS heat flux (h_2) predicted by the sets of nonlinear and linear SGS models is less than 2% and 8% of the resolved wall-normal turbulent heat flux, respectively. At the resolved scale, the difference between these two sets of SGS models is relatively more distinguishable in terms of the quantities related to the temperature field, especially in the cold wall region where the turbulent effect is the strongest due to the existence of buoyancy. It is found in the numerical simulation that the performance of the set of nonlinear SGS models is generally more satisfactory than that of the set of linear SGS models, however, there is also an accompanied slight increase in computational time.

Acknowledgement

The financial support provided by the National Sciences and Engineering Research Council (NSERC) to DJB and BCW, and the Newstead Doctoral Scholarship to JY are gratefully acknowledged.

References

[1] B. Metais, E.R.G. Eckert, Forced, mixed and free convection regimes, ASME J. Heat Transfer. 86 (1964) 295–296.
[2] J.P. Easby, The effect of buoyancy on flow and heat transfer for a gas passing down a vertical pipe at low turbulent Reynolds numbers, Int. J. Heat Mass Transfer. 21 (1978) 791–801.
[3] M. Nakajima, K. Fukui, H. Ueda, T. Mizushina, Buoyancy effects on turbulent transport in combined free and forced convection between vertical parallel plates, Int. J. Heat Mass Transfer. 23 (1980) 1325–1336.
[4] A.M. Abdelmeguid, D.B. Spalding, Turbulent flow and heat transfer in pipes with buoyancy effects, J. Fluid Mech. 94 (1979) 383–400.
[5] H. Tanaka, S. Maruyama, S. Hatano, Combined forced and natural convection heat transfer for upward flow in a uniformly heated vertical pipe, Int. J. Heat Mass Transfer. 30 (1987) 165–174.
[6] N. Kasagi, M. Nishimura, Direct numerical simulation of combined forced and natural turbulent convection in a vertical plane channel, Int. J. Heat Fluid Flow 18 (1997) 88–99.
[7] J.D. Jackson, M.A. Cotton, B.P. Axcell, Studies of mixed convection in vertical tubes, Int. J. Heat Fluid Flow 10 (1989) 2–15.
[8] J.S. Lee, X. Xu, R.H. Pletcher, Large eddy simulation of heated vertical annular pipe flow in fully developed turbulent mixed convection, Int. J. Heat Mass Transfer. 47 (2004) 437–446.
[9] W. Zhang, Q. Chen, Large eddy simulation of natural and mixed convection air flow indoors with two simple filtered dynamic subgrid scale models, Numer. Heat Transfer.: Part A 37 (2000) 447–463.
[10] Z.H. Yan, A numerical study of effect of initial condition on large eddy simulation of thermal plume, Numer. Heat Transfer.: Part B 43 (2003) 167–178.
[11] M. Tyagi, S. Acharya, Large eddy simulations of flow and heat transfer in rotating ribbed duct flows, ASME J. Heat Transfer. 127 (2005) 486–498.
[12] B.-C. Wang, J. Yin, E. Yee, D.J. Bergstrom, A general dynamic linear tensor-diffusivity subgrid-scale heat flux model for large-eddy simulation of turbulent thermal flows, Numer. Heat Transfer.: Part B 51 (2007) 205–227.
[13] M. Germano, U. Piomelli, P. Moin, W.H. Cabot, A dynamic subgrid-scale eddy viscosity model, Phys. Fluids A 3 (1991) 1760–1765.
[14] D.K. Lilly, A proposed modification of the Germano subgrid-scale closure method, Phys. Fluids A 4 (1992) 633–635.
[15] U. Piomelli, High Reynolds number calculations using the dynamic subgrid-scale stress model, Phys. Fluids A 5 (1993) 1484–1490.
[16] B.-C. Wang, D.J. Bergstrom, A general optimal formulation for the dynamic Smagorinsky subgrid-scale stress model, Int. J. Numer. Meth. Fluids 49 (2005) 1359–1389.
[17] T.S. Lund and E.A. Novikov, Parameterization of subgrid-scale stress by the velocity gradient tensor, Annu. Res. Briefs, Center for Turbulence Research, Stanford Univ., 1992, pp. 27–43.
[18] V.C. Wong, A proposed statistical-dynamic closure method for the linear or nonlinear subgrid-scale stresses, Phys. Fluids A 4 (1992) 1080–1082.
[19] B. Kosović, Subgrid-scale modelling for the large-eddy simulation of high-Reynolds-number boundary layers, J. Fluid Mech. 336 (1997) 151–182.
[20] G.S. Winckelmans, A.A. Wray, O.V. Vasilyev, H. Jeanmart, Explicit-filtering large-eddy simulation using the tensor-diffusivity model supplemented by a dynamic Smagorinsky term, Phys. Fluids 13 (2001) 1385–1403.
[21] N. Liu, X. Lu, L. Zhuang, An improved dynamic subgrid-scale model and its application to large eddy simulation of rotating channel flows, Sci. China, Ser. G 47 (2004) 463–476.
[22] B.-C. Wang, D.J. Bergstrom, A dynamic nonlinear subgrid-scale stress model, Phys. Fluids 17 (035109) (2005) 1–15.
[23] C.G. Speziale, On nonlinear k-l and k-ϵ models of turbulence, J. Fluid Mech. 178 (1987) 459–475.
[24] T.B. Gatski, C.G. Speziale, On explicit algebraic stress models for complex turbulent flows, J. Fluid Mech. 254 (1993) 59–78.
[25] B.-C. Wang, E. Yee, D.J. Bergstrom, Geometrical description of the subgrid-scale stress tensor based on Euler axis/angle, AIAA J. 44 (2006) 1106–1110.
[26] P. Moin, K. Squires, W. Cabot, S. Lee, A dynamic subgrid-scale model for compressible turbulence and scalar transport, Phys. Fluids A 3 (1991) 2746–2757.
[27] K. Abe, K. Suga, Towards the development of a Reynolds-averaged algebraic turbulent scalar-flux model, Int. J. Heat Fluid Flow 22 (2001) 19–29.
[28] W.-P. Wang, R.H. Pletcher, On the large eddy simulation of a turbulent channel flow with significant heat transfer, Phys. Fluids 8 (1996) 3354–3366.
[29] R.V.R. Avancha, R.H. Pletcher, Large eddy simulation of the turbulent flow past a backward-facing step with heat transfer and property variations, Int. J. Heat Fluid Flow 23 (2002) 601–614.
[30] L.D. Dailey, N. Wang, R.H. Pletcher, Large eddy simulation of constant heat flux turbulent channel flow with property variations: quasi-developed model and mean flow results, ASME J. Heat Transfer. 125 (2003) 27–38.
[31] L. Wang, X.-Y. Lu, An investigation of turbulent oscillatory heat transfer in channel flows by large eddy simulation, Int. J. Heat Mass Transfer. 47 (2004) 2161–2172.
[32] O. Labbé, P. Sagaut, E. Montreuil, Large-eddy simulation of heat transfer over a backward-facing step, Numer. Heat Transfer.: Part A 42 (2002) 73–90.
[33] J. Pallares, L. Davidson, Large-eddy simulations of turbulent heat transfer in stationary and rotating square ducts, Phys. Fluids 14 (2002) 2804–2816.

[34] A. Keating, U. Piomelli, K. Bremhorst, S. Nešić, Large-eddy simulation of heat transfer downstream of a backward-facing step, J. Turbul. 5 (20) (2004) 1–27.
[35] M.M. Afonso, A. Celani, R. Festa, A. Mazzino, Large-eddy-simulation closures of passive scalar turbulence: a systematic approach, J. Fluid Mech. 496 (2003) 355–364.
[36] J. Yin, B.-C. Wang, and D.J. Bergstrom, LES of buoyant turbulent convection in a vertical slot based on a novel dynamic nonlinear subgrid-scale model, in Proc. 4th Int. Conf. Comput. Heat Mass Transfer., (Paris-Cachan, France), 2005, pp. 51–56.
[37] A. Yoshizawa, A statistical theroy of thermally-driven turbulent shear flows, with the derivation of a subgrid model, J. Phys. Soc. Japan 52 (1983) 1194–1205.
[38] M.V. Salvetti, S. Banerjee, A priori tests of a new dynamic subgrid-scale model for finite-difference large-eddy simulations, Phys. Fluids 7 (1995) 2831–2847.
[39] Y. Zang, R.L. Street, J.R. Koseff, A dynamic mixed subgrid-scale model and its application to turbulent recirculating flows, Phys. Fluids 5 (1993) 3186–3196.
[40] F.A. Jaberi, P.J. Colucci, Large eddy simulation of heat and mass transport in turbulent flows, part 2: scalar field, Int. J. Heat Mass Transfer. 46 (2003) 1827–1840.
[41] F. Porté-Agel, M.B. Parlange, C. Meneveau, W.E. Eichinger, A priori field study of the subgrid-scale heat fluxes and dissipation in the atmospheric surface layer, J. Atoms. Sci. 58 (2001) 2673–2698.
[42] F. Porté-Agel, M. Pahlow, C. Meneveau, M.B. Parlange, Atmospheric stability effect on subgrid-scale physics for large-eddy simulation, Adv. Water Resources 24 (2001) 1085–1102.
[43] H.S. Kang, C. Meneveau, Universality of large eddy simulation model parameters across a turbulent wake behind a heated cylinder, J. Turbul. 3 (32) (2002) 1–27.
[44] S.-H. Peng, L. Davidson, On a subgrid-scale heat flux model for large eddy simulation of turbulent thermal flow, Int. J. Heat Mass Transfer. 45 (2002) 1393–1405.
[45] A. Kuroda, N. Kasagi, M. Hirata, Direct numerical simulation of turbulent plane Couette-Poiseuille flows: effect of mean shear rate on the near-wall turbulence structures, in: F. Durst, N. Kasagi, B.E. Launder, F.W. Schmidt, K. Suzuki, J.H. Whitelaw (Eds.), Proc. Turbul. Shear Flows 9, Springer-Verlag, Berlin, 1995, pp. 241–257.
[46] L. Davidson, D. Čuturić, S.-H. Peng, DNS in a plane vertical channel with and without buoyancy, in: K. Hanjalić, Y. Nagano, M.J. Tummers (Eds.), Turbulence Heat and Mass Transfer 4, Begell House, 2003, pp. 401–408.
[47] K. Horiuti, Roles of non-aligned eigenvectors of strain-rate and subgrid-scale stress tensors in turbulence generation, J. Fluid Mech. 491 (2003) 65–100.
[48] J. Kim, P. Moin, Application of a fractional-Step method to incompressible Navier-Stokes equations, J. Comp. Phys. 59 (1985) 308–323.
[49] C.M. Rhie, W.L. Chow, Numerical Study of the turbulent flow past an isolated airfoil with trailing edge separation, AIAA J. 21 (1983) 1525–1532.
[50] P. Sagaut, R. Grohens, Discrete filters for large eddy simulation, Int. J. Numer. Meth. Fluids 31 (1999) 1195–1220.
[51] Y. Na, T.J. Hanratty, Limiting behavior of turbulent scalar transport close to a wall, Int. J. Heat Mass Transfer. 43 (2000) 1749–1758.